HIGH SPEED DRAG REDUCTION OPTIMIZATION FOR PROJECTILES

Tung Wan, Haw-Chun Chang, Chin-Min Liu
Department of Aerospace Engineering, Tamkang University, Taiwan, Republic of China

Keywords: *high speed flow, drag reduction, jet flow, aerodisk, Kriging method*

Abstract

Drag reduction is one of the important goals for aircraft design or operation, and it is especially true for supersonic or hypersonic flight. We first applying counter-flow jet to impinge upon the opposite supersonic free stream, thus reducing the drag force, then the rear-end jets to decrease the base drag and drag from the expansion waves are also deployed. With the newly defined efficiency parameter, drag reduction of all different cases are calculated and studied, moreover, the effect of different geometric shapes of aerospikes with various disk gap widths on drag reduction are also investigated. This drag reduction efficiency of spiked blunt bodies could be optimized via the Kriging method, and this efficiency would be predominated by the scale of recirculation zone. It appears that both the jet and aerodisk conception considered in this work could find their practical application in future supersonic or hypersonic projectile operation.

1 Introduction

Among all methods to reduce flight vehicle drag the main challenge is still to analyze the detailed drag composition at different flight regimes. For aircraft or missile at supersonic or hypersonic speeds, one of the means to achieve drag reduction is to put counter-flow jet on the nose tip of the body. Many experts studied the counter flow jet problems started from the 1950s [1, 2], and they found it indeed can suit the task. Other researcher even investigated the similar problems by using plasma jets [3], also with different degrees of success but at the expense of electromagnetic complexity. Shang [4] also found that in his analysis the

nonequilibrium and electromagnetic effect of the magnetic field is negligible, and most of the drag reduction is from the viscous-inviscid interaction of the counter-flow jet and thermal energy deposition.

On the other hand, another method for supersonic or hypersonic drag reduction is to set a spike on the nose of the vehicle, thus changing the incoming outer flow field. Investigations have showed that no further reduction of drag can be found once the spike length exceeds approximately 4 times the blunt body diameter [5]. On the contrary, rather than using a pointed spike, mounting an aerodisk at the tip of the spike can provide further drag reduction [6]. Both the spike and disk designs are easy, affordable, and require low energy consumption. It was reported that for some hypersonic flight the drag reduction via the aerospike could reach as high as 78% [7]. Most recently, current authors investigated the optimal drag reduction via the Kriging method for a hypersonic spiked blunt body, and they found the drag could be influenced by the flow patterns including strong bow shock waves, expansion fans, shear layers, flow separation, recirculation regions, compression wave, etc. [8] If the device is just for drag reduction, it will be a good design assuredly. But if shock wave occurs, there is not only large drag force but also high heat transfer needs to be considered. It was found by some researchers that the spike device can not reduce heat flux as efficiently as the counter flow jet does [9, 10], and thus set the cornerstone of current research.

In subsonic flight pressure drag will be generated whenever a flow separation occurs, so there is a low pressure region after the separation points. The unique feature of separation region is that the low flow velocity

and low pressure exist at the same time, thus if more fluid flow inside this low pressure region is provided, then pressure drag will become smaller. For supersonic flow, the flow separation region may also contain low pressure which occurs by expansion wave. A preliminary idea proposed here for supersonic flight is to put a jet on the rear end of the body. By varying the condition of the rear end jet the after-body pressure could also be increased, which means the pressure difference between the front and the back of the body might become smaller.

Jet devices do require extra energy and complicated apparatus to make it works, but its drag reduction potential still attract great interest in the military and space mission applications. For instance, engineers are interested in developing scramjet engine to support the space vehicle and long range missiles [11]. In particular, jet devices could find their usages on capsules against wave drag and reduce heat flux when entering into planetary atmosphere of earth or other planets [12]. In this work we will alter jet parameters and consider hemisphere nose shape in order to test the variation of drag reduction between different cases.

2 Research Background

Aerodynamicists have long researching on the idea of drag reduction; there are numerous methods such as changing aircraft configuration or use different devices or materials. Applications of counter-flow drag reduction techniques were reported to assess performance improvements on aerospace vehicles. If the nose shape is required to be blunt for considerations other than drag, counter-flow jet could be effective in improving the vehicle performance. There is a dimensionless parameter called total pressure ratio that is the ratio of total pressure of the jet and the free stream before bow shock [9]. For a supersonic counter-flow jet at a large angle blunt cone at Mach number 8, there is about 47% drag reduction has been observed when total pressure ratio reaches up to about 75 [11]. That article also points out using counter-flow jet is the most suitable technique to reduce drag force for highly blunted nose shape.

Through experimental [13] or numerical methods, in the past numerous aerodynamicists have investigated the counter-flow jet drag reduction problems by varying different aerodynamic parameters such as the free stream Mach number, the diameter of the cross section area of the jet [14], the mass flow rate of the jet, and the angle of attack with different angles [12], or even use hydrogen or nitrogen as the gas of jet [15]. Their findings seem universal: if the jet conditions are chosen properly, large reductions in drag can be obtained resulting in possible increases in the aircraft performance and its volumetric efficiency.

According to Zhou et al. [9], generally there are two different kinds of modes of the mixing flow field when the counter-flow jet impacts upon the free stream flow. They are the long penetration mode (LPM) and the short penetration mode (SPM). It displays the depth of jet penetration of LPM is several times larger than SPM, thus gives much weaker shock wave [16]. If the pressure ratio is small, the flow field is shown an unsteady condition and it reveals the condition of LPM. Under this condition the more pressure ratio, the more drag reduction. But if the pressure ratio is large enough, it will become SPM and the flow field becomes steady state now. Thus now the more pressure ratio, the less drag reduction it becomes. The maximum drag reduction is about 55.8% in the capsule case when the pressure ratio is at the critical value between LPM and SPM [9].

Josyula et al. [11] recognized the total drag of the flow problem is dominated by wave drag, reverse thrust, and viscous drag, while the reverse thrust could reach 34% of total drag when Mach number is 5.85. If the Mach number down to 3, then the reverse thrust decreases to 16% of total drag and the viscous drag is increasing from 2% to 35%. In fact, viscous drag force has just changed little, which means the total drag is reducing very well. Another finding from their research is that the ogive nose shape is not very effective in the counter-flow drag reduction outcome.

Daso et al. [12] considering a 2.6%-scale Apollo capsule model in Mach 3.48 and 4.0 free streams, and their drag reduction is not satisfactory when the mass flow rate of the

counter-flow jet is not in the proper range. They also employed CFL3D code to propose a physical explanation for the difference in the prediction and the data with the SPM jet case. This could be due to the transient character of the jet penetration modes [16]. In 2006 Venukumar et al. presented their experimental results on a 60 degree apex angle blunt cone at a flow Mach number of 8, about 29% reduction in the drag coefficient has been observed with the injection of a supersonic forward-facing jet [13]. Also from other findings it is recognized that if the total pressure ratio is higher than some critical value, the drag will become larger instead of getting smaller [9]. These results show that if the jet is over strengthened, adverse effect may begin to appear in terms of the drag force.

In 2011 Meyer et al. [14] did a 2-D numerical study of the effects of a counter-flow jet at the nose of a blunt body on wave and skin friction drags for Mach 6.5 flow at 30 km altitude condition. Results of the three different blunt nose diameters are evaluated for jet speeds Mach 2 and 3, and the medium size of the three has the least wave drag. It was discovered that if the ratio of diameters is larger than 63, then the drag force will increase linearly with respect to the jet Mach number. Khamooshi et al. [15] also considered the similar problem but with two NASA codes, SPARK and VULCAN. It is found that the synergistic combination of these two effects (energy deposition and counter-flow jet) always provides for a significant reduction in overall drag on their blunt body.

In recent years, more researchers begin to tackle the complex physical phenomena of the counter-flow jet problems by large-eddy simulation (LES) technique due to the rapid development of the computer resources [17, 18]. At free stream Mach 2.5, they found that the flow behaviors depend mainly on the jet total pressure ratio and can be classified into three typical flow regimes of unstable, stable and transition. The flow field can be quantitatively analyzed using the proper orthogonal decomposition (POD) approach to extract energetic coherent structures, various fundamental mechanisms dictating the complex flow characteristics, including shock/jet

interaction, shock/shear-layer interaction, turbulent shear-layer evolution and feedback mechanisms are clearly observed. There are apparently attachment shock and triple points in the LPM case, and there is a pair of oblique shock and forming an X-type structure. The barrel shock also can be identified.

Similar results also can be found in recent works [19-21], which involved in simple 2-D supersonic flow; several jet configurations caused an increase in the size of the separation bubble, movement of shock toward the exit section, an increase in the oblique shock-wave angle, and a decrease in flow velocity. A hemispherical nose with a sonic opposing jet in free stream of M=2.5, total pressure ratio of 0.816~1.633 are examined, results strongly depends on total pressure ratio, and flow fields oscillates intensely in which the drastic change of the jet structure and the surrounding pressure takes place.

On the other hand, it was long suspected that the benefits of a small jet exhausting rearward might appear to exceed those of the same small jet exhausting forward by itself [1], so preliminary concept proposed here for drag reduction is to put a jet on the rear end of the body. The basic configuration considered here is a rear jet on the classical 2-D backward-facing step, and several studies has been done on this arrangement which include active controls through jet, magnetic field, periodic perturbation, and local forcing, etc. [22-27]

3 Numerical Modeling

3.1 Verification

A standard hemispherical nose configuration was chosen for the counter-flow jet case exactly same as in Chen, et al. [18]. For the rear end jet, the 2-D backward-facing step case by Khan [22] is selected as the benchmark, and after verifying 2-D backward-facing step, later it will be expanded into the 3-D axis-symmetric configuration similar to the case of counter-flow jet. In order to find the best suitable turbulence model to use, the no jet condition will be first tested and verified.

The parameters of counter-flow jet and no jet cases define as follows. The diameter of the

hemispherical nose is 0.05m, and a cylinder connecting behind the nose with the same diameter is added. Jet diameter is 0.005m, one tenth of the hemisphere diameter or cylinder width. Same size of jet will be implemented to the rear end jet cases later. Total temperature of the environment is 294 K, Mach number of free stream is 2.5, specific heat ratio is 1.4, and viscosity coefficient is from Sutherland's formula where the two constant values μ_0 and C in the formula are as the same with the built-in values in Fluent. Reynolds number of free stream is 1470000, Prandtl number is 0.72, and we define the flow as ideal gas, adiabatic and with no radiation heat transfer. On model body surface the stationary, no slip boundary condition is assumed, also ignoring the gravitational force.

For comparison purpose the parameters of rear end or backward-facing step case are same as in [22]. The height of backward-facing step is 11.252 mm, free stream Mach number is 2.5, total pressure is 127553 Pa, total temperature is 362.44 K, Reynolds number is 10050/mm, and the step height is chosen as the characteristic length. Standard condition settings same as the counter-flow problem: specific heat ratio is also 1.4, define the fluid of the environment as ideal gas, and the surface of the model is adiabatic and with no radiation heat transfer. The boundary of the model is the no slip boundary condition, stationary wall, and there is no gravitational force in the flow field.

3.2 Geometry and Mesh

First a 3-D axis-symmetric hemisphere-cylinder configuration is created by Pro-E, then create the meshes with proper boundary conditions selected. The outer boundary is about 50 times of model length and far from the hemisphere-cylinder model itself. Several different hybrid and structured meshes are created and tested, the hybrid mesh has 2754085 cells and the model locates at one-third position near the inlet. As for structured mesh the computational domain considers only a quarter of the model in order to save operation time, but compared to hybrid mesh its quality can be shown by the much smaller values of the dimensionless parameter Y-plus. A side view of hemispherical nose

cylinder with 3360624 cells structured mesh is shown in Fig.1.

As for the 2-D backward-facing step problem its configuration mesh is also the structured type, with similar computational domain layout as the hemisphere-cylinder case. For steady or unsteady state, their meshes are 32160 cells and 86160 cells.
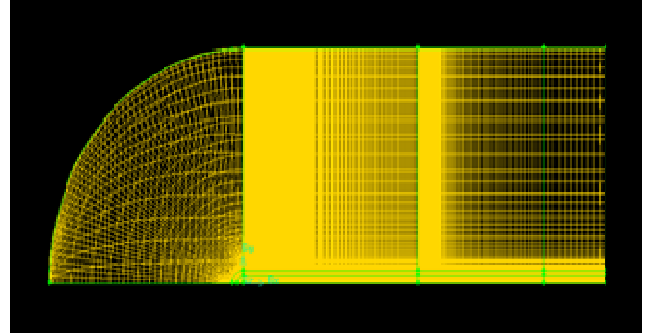

Fig. 1 Side view of hemispherical nose cylinder

3.3 Governing Equations and Solver

In classic physical problems, mass and momentum conservation laws are fundamental assumptions. For fluid dynamics problems these equations are as follows.

$$\frac{\partial \rho}{\partial t} + \vec{\nabla} \cdot (\rho \vec{U}) = 0 \qquad (1)$$

$$\frac{\partial}{\partial t}(\rho \vec{U}) + \vec{\nabla} \cdot (\rho \vec{U}\vec{U}) = -\vec{\nabla}p + \vec{\nabla} \cdot (\tilde{\tau}) + \rho \vec{g} + \vec{F} \qquad (2)$$

Equation (1) is also called continuity and ρ and $\vec{U}$ denote density and velocity, respectively. In equation (2) the third term is pressure gradient, the fourth is stress tensor term, but the gravitational force and the external force will be ignored here.

For supersonic computational the compressible flow form must be imposed, and the energy equation is added as follows,

$$\frac{\partial}{\partial t}(\rho E) + \vec{\nabla} \cdot (\vec{U}(\rho E + p)) = \vec{\nabla} \cdot (K_{eff}\vec{\nabla}T + \tilde{\tau}_{eff} \cdot \vec{U}) \qquad (3)$$

For our supersonic simulations, the realizable k-ε turbulence model and LES (Large Eddy Simulation) method in Fluent code are selected to implement in the above equations. The k-ε turbulence model determines the turbulent length and time scales by solving two equations. Here ideal gas density value is assumed. The value of thermal conductivity is computed by the relationship of Prandtl number,

and the value of thermal conductivity K of the equation is 0.01191934. Viscosity coefficient value is according to Sutherland's formula. First input operating pressure and gauge pressure, let operating pressure is zero at inlet boundary condition, and we define boundary conditions for inlet surface using pressure far field and for outlet surface using pressure outlet. The outer surface of all the control volume is defined as wall. The jet boundary conditions are set on the surface using a specified velocity profile, total temperature, and total pressure. The velocity profile is the usual hyperbolic-tangent function [18] expressed in terms of radial distance and the maximum velocity at the jet axis. Maximum jet velocity range is in between 0.5 and 1.8, but sonic jets happens the most. Since the free stream flows is in the supersonic regime, implicit scheme and Advection Upstream Splitting Method on the density-based solver would be used. Also, in the spatial discretization, we use the Green-Gauss node based in gradient, second order upwind method in flow, turbulent kinetic energy, and specific dissipation rate. Furthermore, all of the criteria of convergence are set as 10^{-4}.

4 Results and Discussion

4.1 Jet Cases

Our verification cases contain two parts: the nose of hemisphere cylinder and the backward-facing step. First the hemisphere nose results are simulated and comparison made with Chen's data [18], for both the no jet and with jet cases. For free stream Mach 2.5, the comparison figure of mean pressure validation of the hemisphere nose location for the no jet and with counter-flow jet conditions, the nose location are expressed in degree, and are from the nose to the shoulder as shown in Fig. 2. The green dot line is our simulation with no jet, and the red dot line is our result with a sonic counter-flow jet which has a total pressure ratio $\mathscr{P}$=1.633.
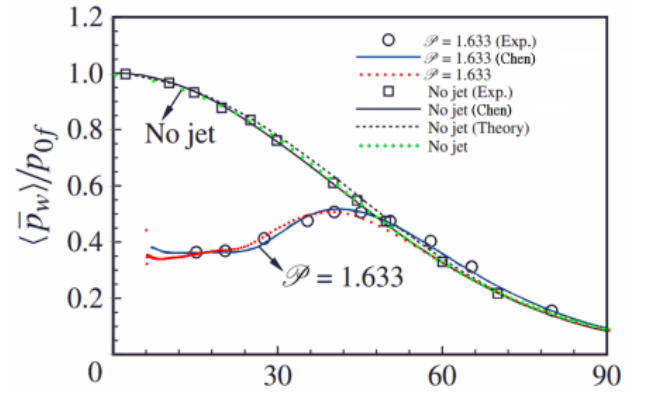

Fig. 2 Mean pressure validation of the hemisphere nose surface for no jet and with counter-flow jet conditions, the nose location are expressed in degree, and are from the nose (0) to the shoulder (90) ($\mathscr{P}$ is total pressure ratio)

In this case the dimensionless parameter Y-plus value is less than 6 in the entire flow field, and in most area it is less than 1, thus the LES module is activated whenever possible. From the figure it is obvious that there is a perfect match between the experiment data and computation results (including ours) in the no jet situation, and in the 20 to 60 degree region the theory deviates slightly due to the inherent inviscid assumption. For the counter-flow case no theoretical data is available, and all the measurement starts at the 10 or 25 degree location due to the detachment of bow shock and unsteady flow behavior. It is observed that our results and Chen's results are differed a little, but overall speaking, both the no jet and counter jet validation simulations seem satisfactory.

Finally the comparison of hemisphere nose pressure drag coefficient for no jet and sonic counter-flow jet situations is made between Chen's results [18] and our results, as shown in Table 1. Total horizontal force is composed of three parts: viscous drag, pressure drag, and the reverse thrust. Due to our calculation, viscous drag only accounts for 1.07% of all the net force in the no jet case. But for the case with counter-flow jet, viscous drag now accounts for 0.99%, pressure drag 91.356%, and reverse thrust 7.653%. According to this comparison, a more than 40% major pressure drag coefficient reduction is observed for both Chen's and our results. Ours is slightly less, 1.903% in terms of absolute total drag coefficient or 4.265% in

terms of relative comparison between the two groups. This seems a direct consequence of discrepancy between the two pressure lines shown in Fig. 2.

Table 1 Comparison of hemisphere nose pressure drag coefficient for no jet and sonic counter-flow jet situations

	Chen's results	Our results	The error with Chen
No jet	0.98572	0.99326	0.765%
Pressure ratio = 1.633	0.54592	0.56900	4.229%
Pressure drag reduction	44.617%	42.714%	4.265%

The second part of validation is the 2-D backward-facing step problem at the same free stream Mach 2.5, this case is chosen with the purpose of future rear end jet addition. Fig. 3 shows the comparison of pressure distribution vs. axial distance for this backward-facing step, which is at the 0.1 m location. The experiment and computation data are taken from [22], and steady and unsteady results are current work. Here the flow solver coupled with the realizable k-ε turbulence model is implemented. It is shown an excellent agreement between current study and the earlier experiment data, especially at the 0.125m position, and almost a perfect match of the steady and unsteady solution, which imply we could employ the fastest solver of the two.
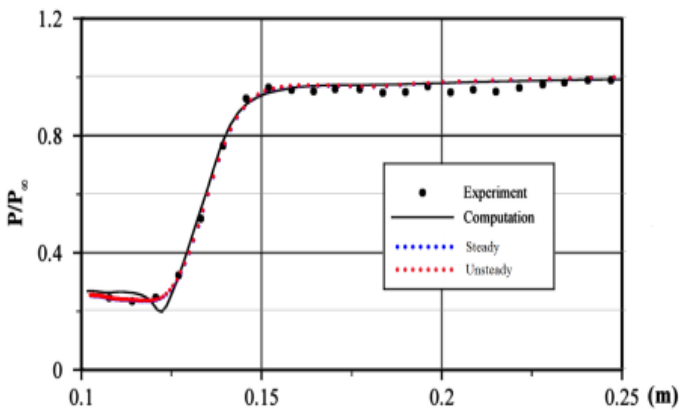
application, the 2-D step geometry is further modified into a 3-D configuration by giving it certain thickness and centerline (or wall) downstream in the middle. Results show that there is only little difference between the "with wall" or "without wall" situations, which implies this test case will be meaningful for later projectile rear end jet application. Now the next goal is to do the grid convergence test for the same 2-D backward-facing step, two structured type mesh system are created with 32160 cells and 86160 cells. Fig. 4 shows very close agreement between the two, although the finer grids do show a little closer behavior to the experiment. Later another 154560 cells grid has also put into test, and it is found that there is no manifest difference in the pressure distribution compared with results from the 86160 cells mesh system. The upstream boundary layer, downstream free shear layer right next to the dividing streamline, and the captured recirculation region in the Mach contour is clearly observed. Also the pressure contour diagram illustration of supersonic features such as expansion fan and reattachment shock is quite obvious. So we can conclude that for the 2-D backward-facing step problem, the reliability of this numerical tool which includes AUSM implicit scheme, realizable k-ε turbulence model, and structured mesh can indeed fulfill the task qualitatively and quantitatively.
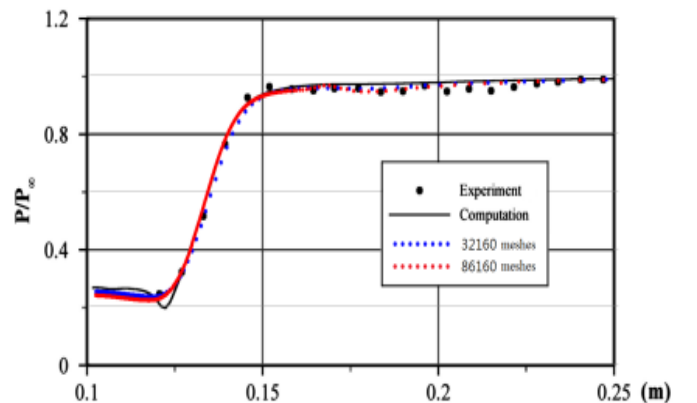

Fig. 3 Comparison of pressure distribution vs. axial distance for 2-D backward-facing step, step locates at 0.1 m

Fig. 4 Mesh convergence test for 2-D backward-facing step pressure distribution

To test the validity of this 2-D backward-facing step for future 3-D confirmation

For the hemispherical nose case, the same LES solver scheme and meshes has been applied to six different counter-flow jet

conditions by varying the jet speed, total pressure ratio, and static pressure. All the results are shown in Table 2. Here we define C_T as thrust coefficient; $C_{D\text{ total}}$ is total drag coefficient, their equations are shown in (4) and (5). Here the same time step is used, and the total pressure ratio is computed from given jet speed. It is found that if the counter-flow jet speed and total pressure ratio increase, then the bow shock will be pushed further upstream and become weaker, pressure drag will decrease, thus the drag reduction amount will become larger.

$$C_T = \frac{\dot{m}v_j + (P_j - P_\infty)A_j}{\frac{1}{2}\rho_\infty v^2 A_b} \quad (4)$$

$$C_{D\text{ total}} = C_D - C_T \quad (5)$$

We can also compute energy consumption for all six cases, if P_{E_k} is kinetic energy per unit second, P_{work} is work per second, and P_{work} is total power. Their relationship is as below:

$$P_{total} = P_{E_k} + P_{work} = \frac{1}{2}\dot{m}v^2 + \Delta p_0 \dot{\forall} \quad (6)$$

where p_0 is total pressure and $\dot{\forall}$ is volume per unit second.

This equation has only two terms if we assume the flow gone through adiabatic and isentropic process when we supply energy to the flow. The first term is kinetic energy term exists due to velocity, and the second term is related to work. If change of total pressure of the fluid flow is needed, we can do work on it, and $\Delta p_0 = p_{0j} - p_{0f}$ means if the total pressure ratio equal to 1, the second term will become zero. Lastly, in order to check the effectiveness of all different cases, a new parameter called efficiency factor is created and defines as the ratio of drag reduction and total power, which is the larger the better. We give it a symbol η and the results are shown in the final row of Table 2, where subscript f represents forebody.

Table 2 Comparison of hemispherical nose for different counter-flow jet conditions

	No jet	Case1	Case 2	Case 3	Case 4	Case 5	Case 6
M_j	-	1	1.2	0.8	1.2	0.8	1
$P_{0j} / P_{0\infty}$	-	1.633	2.093	1.315	1.633	1.633	2
P_j (Pa)	-	253713	253791	253720	198049	315062	310676
$(\dot{m}/A)_j$ (kg/m²s)	-	1132.00	1407.75	878.03	1098.56	1090.32	1386.15
$C_{D,f}$	1.0393	0.5217	0.4438	0.5481	0.4970	0.4931	0.4625
$C_{T,f}$	-	-0.0786	-0.0994	-0.0616	-0.0770	-0.0770	-0.0967
$C_{D,total}$	1.0393	0.6003	0.5432	0.6097	0.5740	0.5701	0.5592
Drag reduction	-	42.24%	47.73%	41.34%	44.77%	45.15%	46.19%
P_{E_k} (kJ/s)	-	1.09420	1.82560	0.57785	1.42463	0.71756	1.33987
P_{work} (kJ/s)	-	1.31448	2.60171	0.54457	1.56672	1.06244	2.02159
P_{total} (kJ/s)	-	2.40868	4.42731	1.12229	2.99135	1.77999	3.36146
η (s/kJ)	-	0.1754	0.1078	0.3684	0.1497	0.2537	0.1374

The mean pressure distribution results of these six cases are shown in Fig. 5, and remembers here Cases 2, 3 and 6 do not possess the 1.633 total pressure ratios. It seems all six cases showing similar behavior in mean pressure on the hemisphere surface, which is not too surprising since mean value tends to rule out any individual irregularities.
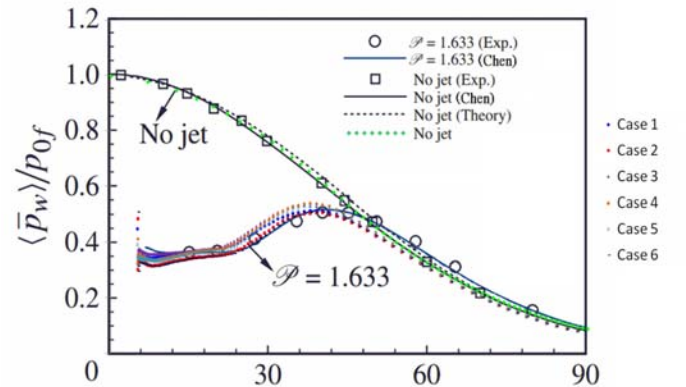

Fig. 5 Mean pressure distribution of the hemisphere nose surface for different counter-flow jet conditions

Besides the hemisphere cylinder and the rear end cases with or without jets, now we can proceed to tackle the more realistic slender projectile configuration which has a fineness ratio of 14.5, and the nose length is the hemisphere radius. For comparison purpose, we employed the same type of mesh system, flow solver, turbulence model, boundary conditions set up including the jet size as the rear end jet

case. First we notice that the total drag coefficient has shrink to become 0.28709 in the no jet condition, naturally it's a consequence of the body slenderness. Then it is observed that the sonic counter-flow jet create a larger drag coefficient C_D value than the supersonic 1.2 Mach counter-flow jet case, but the negative thrust coefficient C_T contribution is less, so the net result is 8.60% drag reduction, slightly larger than the supersonic Mach 1.2 counter jet's drag reduction contribution of 6.35%. These drag reduction are much less than the earlier hemisphere nose Cases 1 and 2 shown in Table 2, which is mainly due to the body shape influence, or the contribution of wave drag to the total drag. It is also interesting to know that now for this slender projectile, its total power is greatly increased, but the drag reduction percentage become much less. So the efficiency factor turned into rather small values, although the sonic counter jet still is much more efficient than the other Mach 1.2 counters jet condition. Remember here the free stream condition is Mach 2.5, a very representative supersonic flight speed.

Table 3 Projectile performance parameters with both counter-flow and rear end jets

	No jet	Case 1	Case 2
Configuration	Hemisphere	Hemisphere	Trumpet-like
$M_{j,f}$	-	1.2	1.5
$P_{0j,f} / P_{0\infty}$	-	2.093	1
$P_{j,f}$ (Pa)	-	172011	54288
$(\dot{m}/A)_{j,f}$ (kg/m²s)	-	740.9711	310.1599
$M_{j,r}$	-	1	1
$P_{0j,r} / P_{0\infty}$	-	1	1
$P_{j,r}$ (Pa)	-	105283	105283
$(\dot{m}/A)_{j,r}$ (kg/m²s)	-	364.7998	364.7998
C_D	0.28709	0.14579	0.16643
$C_{T,f}$	-	-0.09937	-0.04186
$C_{T,r}$	-	4.72260	4.72260
$C_{D\,total}$	0.28709	-4.47744	-4.51431
Drag reduction	-	1659.59%	1672.44%
$P_{E_{k,f}}$ (kJ/s)	-	25.49263	14.81040
$P_{work,f}$ (kJ/s)	-	36.331	0
$P_{E_{k,r}}$ (kJ/s)	-	935.49209	935.49209
$P_{work,r}$ (kJ/s)	-	0	0
P_{total} (kJ/s)	-	997.31572	950.30249
η (s/kJ)	-	0.01664	0.01760

Finally, a single condition is simulated for the same projectile with both the nose counter-flow jet and a rear end jet in Table 3. The counter-flow jet is Mach 1.2 and has a total pressure ratio of 2.093, while both the Mach number and total pressure ratio are one for the rear end jet. Remember subscripts f represents forebody and r is rear end. Also from the definition of total power, the net efficiency factor is 0.01664 and shows a great resemblance to the single rear end jet condition. This finding seems justified the long suspected hypothesis that the benefit of a rear end jet might appear to exceed those of the counter-flow jet.

4.2 Aerodisk Cases

Now for the hypersonic regime, if the device is just for drag reduction, it will be a good design assuredly. But if shock wave occurs, there is not only large drag force but also high heat transfer needs to be considered. It was found that the spike device can not reduce heat flux as efficiently as the counter flow jet does, and thus set the cornerstone of current research. In this work, we investigate the effect of different geometric shapes of aerodisks with various disk gap widths on drag reduction. Accordingly, a series of numerical simulation work was implemented to find the behavior as to high speed flow over aerodisked projectiles. Moreover, the drag reduction efficiency of blunt bodies would be optimized via the Kriging method.

The Kriging method, a kind of surrogate-based optimization scheme, and have used quite efficiently in recent aerodynamic design arena. In this work it was utilized to predict the drag coefficient of unknown spiked blunt body by an archive of configuration design parameters and drag coefficients. The basis function of Kriging method is shown in the following equation, in this case, x denotes the L_1/D (i.e., sample data) and y denotes the total drag coefficients (i.e., observed responses). In this prediction, θ and p would be set as 0.425 and 2, respectively.

$$\psi^{(i)} = exp\left(-\sum_{j=1}^{k} \Theta_j \left| x_j^{(i)} - x_j \right|^{P_j}\right) \quad (7)$$

The Kriging prediction function is demonstrated as

$$\hat{y}(x) = \hat{u} + \boldsymbol{\psi}^T \boldsymbol{\Psi}^{-1}(\mathbf{y} - \mathbf{1}\hat{u}) \qquad (8)$$

where

$$\hat{u} = \frac{\mathbf{1}^T \boldsymbol{\Psi}^{-1} \mathbf{y}}{\mathbf{1}^T \boldsymbol{\Psi}^{-1} \mathbf{1}} \qquad (9)$$

Accuracy of the Kriging model is depending on the numbers of the sample data. As our experience show: if the sample points are enough, then we can find more accurate Kriging model. As in the same single objective case, multi-objective must find the sample points first, and then use Kriging model to find the maximum or minimum values.

From the results obtained, we found the drag could be influenced by the flow patterns including strong bow shock waves, expansion fans, shear layers, flow separation, recirculation regions, compression wave, etc. The bow shock (i.e., conical shock or foreshock) emits from the aerospike and covers the whole hemispherical body. The separation point along the aerospike will influence the pressure and temperature distributions along the main body surface, which counts on the turbulence model and related parameter settings. In terms of the drag components, the pressure drag is the predominant role in both the aerodisk and the blunt main body; however, the viscous drag would be the minor part in the total drag of all spiked blunt bodies. For models with same spike length, then the broader the gap width, the less the total drag. For the models studied, we found that the drag on the disked blunt bodies is much lower than the disked off one. The drag reduction efficiency especially would be predominated by the scale of recirculation zone, which increases as both the aerodisk length and the gap size of aerodisk increase. Hence, the performance of drag diminution will depend on the design parameters such as projectile configurations, length, and tip geometric shapes. The design parameters of the spiked blunt body configurations are shown in Figs. 6-8 and in Table 4 and the gap corner has been smoothly curved in order to avoid any aerodynamic heating possibility. It appears that the aerodisk gap conception considered in this work can found their practical application in future high speed projectile operation.
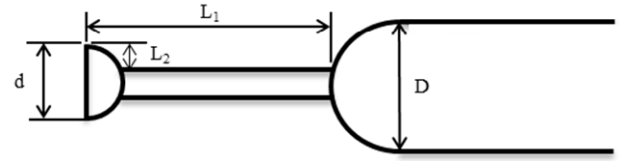

Fig. 6 Prototype model of spiked blunt body

Fig. 7 Prototype model of spiked blunt body with gap

Table 4 The dimensions of investigation cases

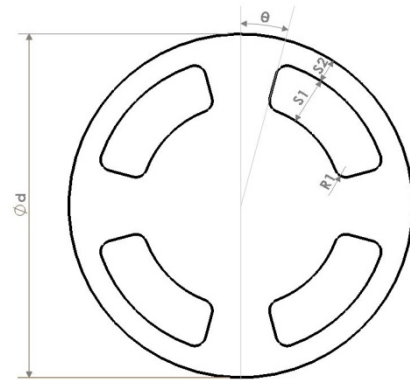| D	0.07620 m
d	0.03048 m
L_1/D	1.5, 2.0, 2.5, 3.0, 3.5, 4.0
L_2	0.01048 m
S_1/L_2	0, 0.2, 0.4, 0.6
S_{2min}	0.002095 m
θ	15°

Fig. 8 Design details of aerodisk with gap and $S_1/L_2=0.4$

The design parameter is twofold. First, the aerospikes would vary with different length-to-main-body-diameter ratios (i.e., $L_1/D=1.5$–4.0). Second, several gap-size-to-disk-length ratios (S_1/L_2) for the gaps amongst the aerodisks would range from 0 up to 0.6. We found the

total drag of same L_1/D would decrease as the S_1/L_2 increase, in addition, the difference between the drag coefficients of two different spike length sizes would diminish on account of the effect of increasing the spike length on drag reduction is fallen gradually. Besides, the pressure drag coefficients demonstrate the total drag force is most occupied by pressure drag force, and it is obviously that the total drag coefficient distributions with different spike configurations correspond to the distributions of pressure drag coefficients.

It is very interesting to note that the longer spike length could lead to the flow separation point away from the main body surface and most importantly, both the compression wave and the flow recirculation zones enlarge as the aerospike length increases, thus the larger portion of the main body surface would be cloaked by them, consequently, the total drag of longer spiked blunt body would be lower than which of previous relatively shorter one. With the purpose of reducing the pressure drag in different gap widths, the aerodisks with varying dimensions of gap would be fixed atop the aerospikes of the hypersonic blunt bodies would be also another crucial design point. The chief capability of aerospike coupled with aerodisks is to give rise to the separation flow and reduce drag force via dispersing the strong shock wave into much weaker shock wave.

For the sake of design, we would like to acquire the total drag coefficient of spike blunt body with $L_1/D=5$ and $S_1/L_2=0.6$, thus we can make use of the matrices X and Y from the length-to-main-body-diameter ratio (L_1/D) and total drag coefficient, respectively. From the results, we obtained the total drag coefficient of the prediction model is 0.06954 and the error relative to the CFD simulation one is 0.008629 % and the drag reduction efficiency is up to 68.4 %, that is, the performance of which is better than the spiked blunt body with $L_1/D=4$ and same gap dimension because the recirculation zone for $L_1/D=5$ is larger than which for $L_1/D=4$. Since the estimated value gained by Kriging method is much closer to simulated one, thereby Kriging method is indeed a reliable and practical optimization approach.
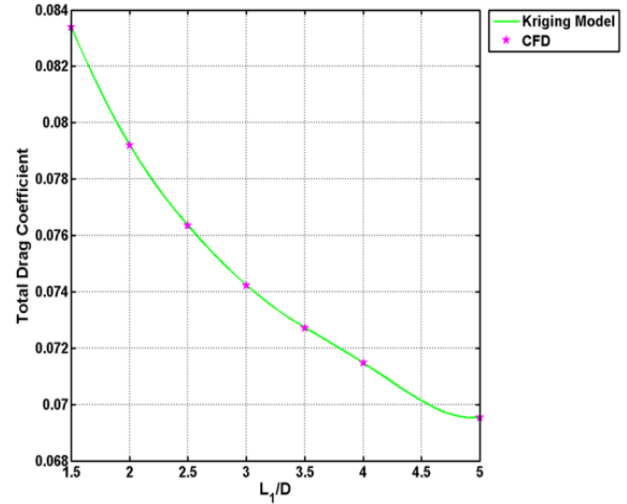

Fig. 9 Prediction of total drag coefficient via Kriging method

5 Conclusions

Several different configurations have been computed at free stream Mach 2.5 condition with numerous strengths of jet at nose and rear end locations, which include a short hemisphere cylinder, a 3-D cylindrical base, and a slender projectile. Standard counter-flow jet and backward-facing step problems are first tested and validated with satisfactory results, then the three configurations simulations are compared with thrust coefficient, total drag coefficient, total power, and the newly defined efficiency factor η. The main findings in this work are first indeed the nose counter-flow jet can have major drag reduction effect, but the effectiveness will greatly depend on the vehicle body shape and the jet strength. Secondly, a rear end jet can provide direct thrust, and it's proved that the benefit of a rear end jet might exceed those of the counter-flow jet for our slender projectile. Unlike aero-spiked nose, counter-flow jet required large amount of energy to supply the continuous jet mass in the harsh supersonic environment, not to mention the problems related to the complicated apparatus in order to provide the counter jet. So it might be fair to say the efficiency factor is physically more meaningful than the drag reduction itself.

Also for hypersonic blunt body with aerospikes, we could identify that our numerical simulations agree with the validation cases very well. For spike off, the total drag is much higher

than spike on case as a result of the presence of strong bow shock. In addition, the temperature distribution of spike off is much higher than spike on one. On the other hand, an innovative smooth gaps on the aerodisk was proposed in this research and from the outcome, we argued that the minimum drag comes about at the max gap (i.e., S_1/L_2=0.6) under same aerospike length. Besides, the mechanism of drag reduction can be predominated by effective body and the effect of recirculation. More importantly, the efficiency of drag reduction would decrease as the sizes of spike and gap increase.

From the results obtained, we found the drag could be influenced by the flow patterns including strong bow shock waves, expansion fans, shear layers, flow separation, recirculation regions, compression wave, etc. The bow shock (i.e., conical shock or foreshock) emits from the aerospike and covers the whole hemispherical body. The separation point along the aerospike will influence the pressure and temperature distributions along the main body surface, which counts on the turbulence model and related parameter settings. In terms of the drag components, the pressure drag is the predominant role in both the aerodisk and the blunt main body. For models with same spike length, then the broader the gap width, the less the total drag. In this work, we found that the maximum drag reduction for same spike length would be found at widest gap. Thereby, the drag reduction performance attained by both the aerospike and aerodisk would rely on the trade-off between the spike length and the gap width.

References

[1] Love, E.S., The Effects of a Small Jet of Air Exhausting from the Nose of a Body of Revolution in Supersonic Flow, National Advisory Committee for Aeronautics, Research Memorandum L52I19a, November 1952.

[2] Finley, P.J., The Flow of a Jet from a Body Opposing a Supersonic Free Stream, *Journal of Fluid Mechanics*, Vol. 26, part 2, December 1966, pp. 337-368.

[3] Shang, J.S., Recent Research in Magneto-Aerodynamics, *Progress in Aerospace Sciences*, Vol. 37, 2001, pp.1-20.

[4] Shang, J.S., Plasma Injection for Hypersonic Blunt-Body Drag Reduction, *AIAA Journal*, Vol. 40, No. 6, June 2002, pp. 1178-1186.

[5] Gauer, M. and A. Paull, "Numerical Investigation of a Spiked Blunt Nose Cone at Hypersonic Speeds," Journal of Spacecraft and Rockets, Vol. 45, No. 3, 2008.

[6] Ahmed, M.Y.M. and N. Qin, "Drag Reduction Using Aerodisks for Hypersonic Hemispherical Bodies," Journal of Spacecraft and Rockets, Vol. 47, No. 1, 2010, pp. 62-80.

[7] Kalimuthu, R., R.C. Mehta, and E. Rathakrishnan, Drag Reduction for Spike Attached to Blunt-Nosed Body at Mach 6, *Journal of Spacecraft and Rockets*, Vol. 47, No. 1, 2010, pp. 219-222.

[8] Wan, T. and Chin-Min Liu, Drag Reduction Optimization for Hypersonic Blunt Body with Aerospikes, *Journal of Aeronautics & Aerospace Engineering*, Vol. 6, No. 4, 2017, DOI: 10.4172/2168-9792.1000200.

[9] Zhou, C.Y., W.Y. Ji, and P. Xie, Numerical Investigation on the Drag and Heat Flux Reduction of a Supersonic Reentry Capsule with a Counter-flow Jet, *Information Technology Journal*, Vol. 11, 2012, pp. 1705-1713.

[10] Josyula, E., M. Pinney, and W.B. Blake, Applications of a Counterflow Drag Reduction Technique in High-Speed Systems, *Journal of Spacecraft and Rockets*, Vol. 39, No. 4, 2002.

[11] Venukumar, B., G. Jagadeesh, and K.P.J. Reddy, Counterflow Drag Reduction by Supersonic Jet for a Blunt Body in Hypersonic Flow, *Physics of Fluids*, Vol. 18, 2006.

[12] Daso, E.O., V.E. Pritchett, T.S. Wang, D.K. Ota, I.M. Blankson, and A.H. Auslender, Dynamics of Shock Dispersion and Interactions in Supersonic Freestreams with Counterflowing Jets, *AIAA Journal*, Vol. 47, No. 6, 2009, pp. 1313-1326.

[13] Venukumar, B. and K.P.J. Reddy, Experiments Investigation of Drag Reduction by Forward Facing High Speed Gas Jet for a Large Angle Blunt Cone at Mach 8, *Sadhana*, Vol. 32, Parts 1 & 2, February-April 2007, pp. 123-131.

[14] Meyer, B., H.F. Nelson, and D.W. Riggins, Hypersonic Drag and Heat-Transfer Reduction Using a Forward-Facing Jet, *Journal of Aircraft*, Vol. 38, No. 4, July-August 2011, pp. 680-686.

[15] Khamooshi, A., T. Taylor, and D.W. Riggins, Drag and Heat Transfer Reductions in High-Speed Flows, *AIAA Journal*, Vol. 45, No. 10, 2007, pp. 2401-2413.

[16] Daso, E.O., W. Beaulieu, and J.O. Hager, Prediction of Drag Reduction in Supersonic and Hypersonic Flows with Counterflow Jets, *AIAA Paper 2002-5115*, 2002.

[17] Chen, L.W., C.T. Xu, and X.Y. Lu, Large-Eddy Simulation of Opposing-Jet-Perturbed Supersonic Flows Past a Hemispherical Nose, *Modern Physics Letters B*, Vol. 24, No. 13, 2010, pp. 1287-1290.

[18] Chen, L.W., G.L. Wang, and X.Y. Lu, Numerical Investigation of a Jet from a Blunt Body Opposing a Supersonic Flow, *Journal of Fluid Mechanics*, Vol. 684, 2011, pp. 85-110.

[19] Fujita, M., Axisymmetric Oscillations of an Opposing Jet from a Hemispherical Nose, *AIAA Journal*, Vol. 33, 1995, pp. 1850-1856.

[20] Venkatachari, B.S., Y. Ito, G. Cheng, and Chau-Lyan Chang, Numerical Investigation of the Interaction of Counterflowing Jets and Supersonic Capsule Flows, *AIAA Journal*, 2011.

[21] Lohner, R., and Baum, J., On the Drag Efficiency of Counterjets in Low Supersonic Flow, *AIAA Paper 2015-0069*, 2015.

[22] Khan, O.U. and K.A. Hoffmann, Flow Control over a Backward-Facing Step with Application of a Magnetic Field, *Journal of Spacecraft and Rockets*, Vol. 45, No. 2, 2008, pp. 255-263.

[23] Emami-Naeini, A., S.A. McCabe, D. de Roover, J. L. Ebert, and R. Le Kosut, Active Control of Flow over a Backward-Facing Step, *Proceedings of the 44th IEEE Conference on Decision and Control, and the European Control Conference 2005*.

[24] Mehrez, Z., M. Bouterra, A.E. Cafsi, A. Belghith, and P.L. Quere, Active Control of Flow Behind a Backward Facing Step by Using a Periodic Perturbation, *ARPN Journal of Engineering and Applied Sciences*, Vol. 5, No. 2, 2010, pp. 7366-7371.

[25] Behrens, A.A., J.M. Lutz, and P.J. Strykowski, Instantaneous Flame Anchor Measurements Behind a Rearward-Facing Step, *AIAA Journal*, Vol. 47, No. 6, 2009, pp. 1350-1357.

[26] Mehrez, Z., M. Bouterra, A.E. Cafsi, A. Belgith, and P.L. Quere, Mass Transfer Control of a Backward-Facing Step Flow by Local Forcing-Effect of Reynolds Number, *Thermal Science*, Vol. 15, No. 2, 2011, pp. 367-378.

[27] Henning, L. and R. King, Robust Multivariable Closed-Loop Control of a Turbulent Backward-Facing Step Flow, *Journal of Aircraft*, Vol. 44, No. 1, 2007, pp. 201-208.

Contact Author Email Address

twan@mail.tku.edu.tw

Copyright Statement